A New Study of the Mediterranean Outflow, Air–Sea Interactions, and Meddies Using Multisensor Data

XIAO-HAI YAN* AND YOUNG-HEON JO

Graduate College of Marine Studies, University of Delaware, Newark, Delaware

W. TIMOTHY LIU

Jet Propulsion Laboratory, California Institute of Technology, Pasadena, California

MING-XIA HE

Ocean Remote Sensing Institute, Ocean University of Qingdao, Qingdao, China

ABSTRACT

Previous studies of the Mediterranean Sea outflow and meddies (O&M) were limited by the poor spatial and temporal resolution of conventional in situ observations as well as the confinement of satellite observations to the ocean's surface. Accordingly, little is known about the formation and transport of meddies and the spatial and temporal variation of O&M trajectories, which are located, on average, at a depth of 1000 m. However, a new remote sensing method has been developed by the authors to observe and study the O&M through unique approaches in satellite multisensor data integration analyses. Satellite altimeter, scatterometer, infrared satellite imagery, and XBT data were used to detect and calculate the trajectories and the relative transport of the O&M (January 1993–December 2002). Two experiments [covering 1993–95: A Mediterranean Undercurrent Seeding Experiment (AMUSE) and Structures des Echanges Mer–Atmosphère, Propriétés des Hétérogénéités Océaniques: Recherche Expérimentale (SEMAPHORE)] and XBT temperature measurements were used to directly validate the method presented herein. The monthly mean features derived from floats and XBTs for multiple meddies and the results of the presented method were significantly correlated based on a statistical chi-square test. In addition, the complex singular value decomposition method was used to identify the propagating features and their phase speeds. It was found that saltier water from the Mediterranean Sea was transported into the North Atlantic Ocean over the Strait of Gibraltar in boreal spring and summer relative to boreal autumn and winter. Streamfunctions using altimetry, and time–frequency energy distributions using the Hilbert–Huang transform, were computed to evaluate the meddy interactions with the sea surface variation. Since the O&M play a significant role in carrying salty water from the Mediterranean Sea into the Atlantic, such new knowledge about their trajectories, transport, and life histories is important to the understanding of their mixing and interaction with North Atlantic water. This may lead to a better understanding of the global ocean circulation and global climate change.

1. Introduction

One of the most interesting and prominent features of the North Atlantic Ocean is the salt tongues originating from an exchange flow between the Mediterranean Sea and the Atlantic through the Strait of Gibraltar. The Mediterranean outflow through the strait is denser than Atlantic water because of its higher salt content. Evaporation in the Mediterranean Sea raises the salinity to around 38.4 psu, as compared with 36.4 psu in the eastern North Atlantic. After leaving the strait under the incoming, lighter North Atlantic water, the Mediterranean outflow sinks and turns to the right, because of the Coriolis force, following the continental slope off Spain and Portugal. Eventually, this water leaves the coast and spreads into the middle North At-

lantic, forming a tongue of salty water. This generates clockwise-rotating eddies. These Mediterranean eddies, or meddies (McDowell and Rossby 1978) as they are often called, are rapidly rotating double-convex lenses that contain a warm, highly saline core of Mediterranean water 200–1000 m thick. Relative to the background water in the Canary Basin, meddy salinity and temperature anomalies can be 1 psu and 2°–4°C higher, respectively (Bower et al. 1997; Richardson et al. 2000). Because of the water differences between a meddy and the North Atlantic, isopycnal amplitude reaches 6 cm (Stammer et al. 1991; Tychensky and Carton 1998). A meddy has a typical diameter of approximately 100 km and, on average, is located at a depth of 1000 m. Most meddy observations have been found in the Canary Basin (Armi and Zenk 1984; Käse and Zenk 1987) and in the eastern North Atlantic (Armi and Stommel 1983; Pingree and Le Cann 1993; Bower et al. 1997).

Generally speaking, most remotely sensed oceanographic observations are confined to either the sea surface or to the upper mixed layer, but this limitation is not always true. Yan et al. (1990, 1991a,b) and Yan and Okubo (1992) developed methods to infer the upper-ocean mixed layer depths from multisensor satellite data. Furthermore, Stammer et al. (1991) applied *Geosat* Exact Repeat Mission (GERM) altimeter data to investigate the possible surface signal of meddies. They compared the dynamic topography calculated from hydrographic data with samples from an eddy-resolving station network in the Iberian Basin. Although they were unable to detect meddies from space alone (in the absence of accompanying in situ data), they identified the possible surface meddy signals using both GERM altimeter data and hydrographic data. Similarly, Tokmakian and Challenor (1993) also reported that individual eddies or meddies cannot be identified using GERM altimeter data, but the Azores Current could be.

The possible surface meddy signals in the altimeter data were distinguishable from the background (e.g., fronts, currents, and eddies) field determined from hydrographic data. The formation and early stages of development of anticyclonic mesoscale eddies with a core of slope water were observed in a study by Pingree and Le Cann (1992). One of these slope water oceanic eddies ("swoddie") was seen in infrared (IR) satellite imagery. Pingree and Le Cann (1993) also showed evidence of a shallow meddy (smeddy) at 700-m depth on the southern Tagus Abyssal Plain from IR satellite imagery. However, IR imagery only enables one to monitor the early stage of the possible meddies, when there is a sea surface temperature (SST) gradient, and when meddies are located in a shallow region. The early stage, which occurs close to the sharp dropoff of the

continental shelf, can be distinguished from the later stages by the location of the formation of the meddies. Oliveira et al. (2000) showed these eddylike features using a sequence of six SST images and altimetry data and compared these features with float data. They found that the IR image of the meddies during the winter/spring is clearer than other seasons when coastal upwelling is relaxed.

We hereby report a new method to study the Mediterranean outflow and meddies (O&M) by analysis of altimeter, scatterometer, IR satellite imagery, and expendable bathythermography (XBT) data. We compute the vertical sea level difference: $\Delta \eta' = \eta'_{\text{Total}} - \eta'_{\text{UL}} = \eta'_{\text{Total}} - (\eta'_T + \eta'_S + \eta'_W)$, where η'_{Total} is the deviation of the sea surface topography of the whole vertical water column, which can be measured by altimetry, and η'_{UL} is the sea surface variation in the upper layer (400 m) due to thermal expansion η'_T, salt expansion η'_S, and the wind stress η'_W. Because it is impossible to decompose the sea surface height anomaly into each corresponding signal, such as η'_T, η'_S, and η'_W, we estimated them using individual measurements, and then removed the signals of η'_T, η'_S, and η'_W from the total sea level variation η'_{Total}. Therefore, we consider the rest of the signal as the meddy signals $|\Delta \eta'|$, and this sea level difference, $|\Delta \eta'|$, is used to distinguish meddy signals from the background field in the upper layer. Thus, the meddy signals are not necessarily individual meddies, but actually multiple meddies at a 400-m isopycnal surface.

It is worth noting that our results differ from those of Stammer et al. (1991) and others referenced above. To remove the upper-layer variation (include the Azores front) from the many other signals in the altimeter data, we differentiated the surface meddy signals from the thermal-, salinity-, and wind-induced sea level variations of the upper layer (0–400 m). By removing the other signals in the altimeter data, one can, thus, identify the signal of the O&M. In addition, one can even monitor the meddies, not only in the early stages near the continental shelf, but also in the later stages at greater distances from their origin. The improved methodology developed in this study also permits a longer time scale (because our data record length is longer) than GERM altimeter data and achieves a higher degree of accuracy than those from earlier studies.

The rest of this paper is organized as follows: the method and data are described in section 2. We then introduce the approach for removing the signals of the upper-layer variation in section 3, and we present our O&M signal and validation in section 4. In section 5, the following studies are presented the spatial and temporal variations of the meddies $|\Delta \eta'|$ using complex sin-

gular value decomposition analysis, the relative transport of the Mediterranean outflow, and the interactions between sea level variation determined from the streamfunction and the meddies measured by the floats. Section 6 presents the conclusions.

2. Methods and data

a. Integrated multisensor data analysis (IMSDA)

We used the following algorithm to estimate the meddy signals:

$$\Delta\eta'(T, S, W, X, t) = \left[\eta_{\text{Total}}(T, S, W, X, t) - \frac{1}{K} \sum_{}^{K} \eta_{\text{Total}}(T, S, W, X, t) \right]$$
$$- \left[\eta_{\text{UL}}(T, S, W, X, t) - \frac{1}{K} \sum_{}^{K} \eta_{\text{UL}}(T, S, W, X, t) \right] = \eta'_{\text{Total}} - \eta'_{\text{UL}}, \tag{1}$$

where

$$\eta'_{\text{UL}} = \left[\eta_T(T, X, t) - \frac{1}{K} \sum_{}^{K} \eta_T(T, X, t) \right] + \left[\eta_S(S, X, t) - \frac{1}{K} \sum_{}^{K} \eta_S(S, X, t) \right]$$
$$+ \left[\eta_W(W, X, t) - \frac{1}{K} \sum_{}^{K} \eta_W(W, X, t) \right] \tag{2}$$

and

$$\eta'_{\text{UL}} = \eta'_T + \eta'_S + \eta'_W, \tag{3}$$

where η'_{Total} is the deviation of the sea surface topography, η_{Total}, after removing the long-term mean, which can be measured by satellite altimetry. In addition, T, S, W, X, and t represent temperature, salinity, wind, space, and time in months ($K = 120$ months from January 1993 to December 2002), respectively. The η'_{UL} variation is due to η'_T, η'_S, and η'_W, which can be estimated from temperature measurements from IR satellite imagery and XBTs, salinity measurements from Levitus and Boyer (1994, hereinafter Levitus 94), and scatterometer data from the *European Remote Sensing Satellites-1* and *-2* (*ERS-1/2*), the National Aeronautics and Space Administration (NASA) Scatterometer (NSCAT), and the NASA Quick Scatterometer (QuikSCAT), respectively. A time series of gridded monthly values of the O&M signals with 18-km resolution was developed. This resolution is high enough to resolve mesoscale features [e.g., meddy's horizontal scale (~100-km diameter)].

b. Coupled pattern analysis

Coupled pattern analysis (CPA) provides another means of matching patterns for two separate time-dependent fields, provided the processes underlying the two are simply and directly related. In essence, they are a means of deducing matched pairs of spatial patterns, one for each field, that have a high temporal correlation. This property makes it more attractive than deriving the empirical orthogonal function (EOF) modes of each of the two fields separately and comparing them, mode by mode. This method is effective, though the purely statistical nature of the analysis and the empirical nature of the basis functions for the two fields mean that the EOF modes of the two fields may not be necessarily related to each other. CPA has been used in analyzing climate data (Bretherton et al. 1992), and matching the patterns of variability of SST and atmospheric pressure (Peng and Fyfe 1996; Wallace et al. 1992).

CPA analysis is similar to EOF analysis (Leuliette and Wahr 1999) in that the two fields are decomposed into orthonormal modes:

$$f(x, t) = \sum_{k=1}^{M} \alpha_k(t) u_k(x) \quad \text{and} \tag{4}$$

$$g(x, t) = \sum_{k=1}^{M} \beta_k(t) v_k(x), \tag{5}$$

where u and v are the spatially dependent function of $f(x, t)$ and $g(x, t)$, respectively. Here M is the number of spatial points x.

We defined $f(x, t)$ as η'_T and $g(x, t)$ as the SST anomaly SST' in this study. By determining a regression coefficient between $f(x, t)$ and $g(x, t)$, we estimated a new thermal steric height anomaly from SST'. The details of the application of this methodology are discussed in section 3.

c. Complex singular value decomposition (CSVD)

Barnett (1983) applied complex EOF (CEOF) analysis using a covariance matrix to investigate the interaction of the monsoon and trade wind systems in the Pacific Ocean. In this study, we used CSVD, for which

the covariance matrix is not needed. Using CSVD, one can calculate not only the eigenvalues and eigenvectors, but also the spatial amplitudes, and spatial and temporal phase functions (Susanto et al. 1998). Susanto et al. (1998) defined the spatial $\psi_n(t)$ and temporal $\phi_n(t)$ phase function as shown in (6) and we used that to study the propagating phases of the O&M:

$$\psi_n(t) = \arctan\left\{\frac{\text{Im}[A_n(t)]}{\text{Re}[A_n(t)]}\right\} \quad \text{and}$$

$$\phi_n(t) = \arctan\left\{\frac{\text{Im}[B_n(t)]}{\text{Re}[B_n(t)]}\right\}, \quad (6)$$

where A_n and B_n are the spatial and temporal complex principal components, respectively, and t is time.

d. Hilbert–Huang transform (HHT) and spectra (HHS)

The fundamental idea of time–frequency analysis is to understand and describe situations where the frequency component of a signal is changing in time. The extrinsic mode decomposition (EMD) method is a general method of time–frequency analysis, which is applicable to nonlinear and nonstationary signals. Since the decomposition is based on the local characteristic time scale of the data, it is applicable to nonlinear and nonstationary processes. With the Hilbert transform, the intrinsic mode functions (IMFs) yield instantaneous frequencies, as functions of time that give sharp identification of embedded structures. The main conceptual innovation in this approach is the introduction of the instantaneous frequencies for complicated datasets, which eliminate the need for spurious harmonics to represent nonlinear and nonstationary signals. The essence of the EMD method is to identify the oscillatory modes by their characteristic time scales in the data empirically and, then, decompose the data accordingly. The decomposition of the data into decomposed simple mode functions (SMFs) uses envelopes defined by the local maxima and minima separately. Once the extrema are identified, all the local maxima are connected by a cubic spline as the upper envelope. The procedure is repeated for the local minima to produce the lower envelope. The Hilbert spectrum was designed to apply the HHS to the SMF and construct the energy–frequency–time distribution (Huang et al. 1998). The Hilbert-transformed series has the same amplitude and frequency content as the original real data and also includes phase information that depends on the phase of the original data. The Hilbert transform is useful in calculating instantaneous attributes of a time series, especially the amplitude and frequency. The instanta-

neous amplitude is the amplitude of the complex Hilbert transform; the instantaneous frequency is the time rate of change of the instantaneous phase angle.

e. Sea level anomaly

The series of sea level anomalies (SLA) is obtained from a complete reprocessing of Ocean Topography Experiment (TOPEX)/Poseidon (T/P), *Jason-1*, and *ERS-1/2* satellite data (January 1993–December 2002). (Detailed information about the SLAs can be found online at ftp://ftp.cls.fr/pub/oceano/enact/msla/readme_MSLA_ENACT.htm.) The T/P instrument was replaced by *Jason-1* in August 2002 after its orbit change. *ERS-2* is available from June 1996 to June 2003. *ERS-2* was then replaced by the *Environmental Satellite* (*ENVISAT*). The SLAs were computed using conventional repeat-track analysis. The SLAs are relative to a 7-yr mean (January 1993–January 1999). By removing a 7-yr mean sea level height, we are able to remove the geoid from the altimeter measurements. Accordingly, the bathymetric effects on the altimeter measurements are a minimum. A specific processing is performed to get an *ERS-2* mean consistent with a T/P mean. The SLA is provided on a ⅓ Mercator grid. Resolutions in kilometers in latitude and longitude are thus identical and vary with the cosine of latitude (e.g., from 37 km at the equator to 18.5 km at 60°N/S). To make the same grid points for the O&M signals using Eqs. (1)–(3), we interpolated the SLAs into a 18-km spatial resolution, which is the same resolution as used for the Advanced Very High Resolution Radiometer (AVHRR) SST.

f. Thermal steric height (η_T')

In order to estimate the sea level variation resulting from thermal expansion in the upper layer η_T', the sea surface height anomaly was calculated using monthly mean XBT data acquired from the Joint Environmental Data Analysis (JEDA) Center. This method integrated temperatures through the water column to 400-m depths from January 1993 to December 2002, that is,

$$\eta_T' = \alpha \int_{-400}^{0} \Delta T \, dz - \frac{\alpha}{K} \sum^{K} \int_{-400}^{0} \Delta T \, dz, \quad (7)$$

where ΔT is the temperature difference between two different depths (dz) and α is the thermal expansion coefficient, which is calculated as a function of salinity S and water pressure P, based on empirical measurements (Wilson and Bradley 1966):

$$\alpha = -\frac{1}{\rho_0}\frac{\Delta\rho}{\Delta T}\bigg|(s, p),$$

where ρ_0 is the reference density and $\Delta\rho$ is the density difference between two layers. However, we found that the spatial resolution of XBT data ($2° \times 5°$ latitude–longitude) for the η'_T was not high enough to resolve mesoscale features. To estimate the interpolation error of the XBTs, we determined the correlation and rms differences between optimum interpolation SST and SST derived from XBTs. Its correlation is $O(0.96)$, and the rms differences are 0.5°C, respectively. We believe that the spatial resolution of the XBT data before interpolation into $1° \times 1°$ latitude–longitude is not a problem, because η'_T is supposed to estimate the sea level variation for much larger spatial areas than that of the meddies.

Furthermore, in order to obtain better spatial resolution, we computed a new thermal steric height from the AVHRR SST data (18 km) after applying an empirical regression curve using CPA as demonstrated in the next section. To do that, optimum interpolated sea surface temperature (OISST) with a spatial resolution of a 1° grid, from January 1993 to December 2002, was also used. The OISST was obtained from the National Oceanic and Atmospheric Administration/National Centers for Environmental Prediction (NOAA/NCEP). The monthly optimum interpolation (OI) fields were derived by a linear interpolation of the weekly OI fields to daily fields and then averaging the daily values over a month (Reynolds and Smith 1994). The sources of OISST are based on the Comprehensive Ocean–Atmosphere Data Set and satellite observations. For the AVHRR (18-km resolution), we obtained the data from the Physical Oceanography Distributed Active Archive Center (PO.DAAC) AVHRR Oceans Pathfinder (information online at ftp://podaac.jpl.nasa.gov/pub/sea_surface_temperature/avhrr/pathfinder/).

3. Removal of signals of upper-layer variation from η'_{Total} for the O&M signal ($|\Delta\eta'|$)

A schematic diagram of our method is shown in Fig. 1. Sea level variation due to salinity (temperature) change, using mass conservation and a thickness of 800 m, is about 60 cm (32 cm), with one part per thousand salinity and 2°C differences from the background fluid. These differences were derived from the salt expansion coefficient 7.5×10^{-4} (‰)$^{-1}$ and the thermal expansion coefficient 2.0×10^{-4}°C^{-1}, respectively. One can see the relatively broader isopycnal surface (L) as it moves above the meddy toward the sea surface. Because of this isopycnal compensation, the O&M are not obviously revealed in the η'_{Total} signal at the sea surface.
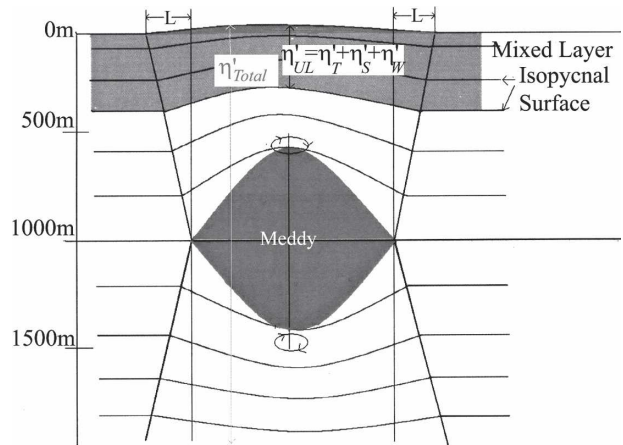

FIG. 1. Conceptual diagram of this study based on the isopycnal surface. The aim of this study is to estimate the isopycnal surface at 400-m depth using multisensor data integration analysis. The isopycnal surface at the sea surface is almost flat; however, at 400-m depth there is a significant change that can be detected.

This is why we cannot always detect a meddy with altimeter data alone. However, the isopycnal surfaces near the meddy resemble the meddy's curved structure. Field measurements of the vertical sections of potential density through the three meddies (Tychensky and Carton 1998, their Plate 6) showed similar features to those in Fig. 1. Comparing the isopycnal surfaces at 1000-m depths, one can see the broader and flatter isopycnal surfaces at the 400-m depths. We cannot see a meddy signal at the sea surface as Stammer et al. (1991) and Tokmakian and Challenor (1993) reported. In addition, two other studies also showed that the hydrographic signature and rotation velocity of the influences of the meddy can be seen in the isopycnal displacements at depths as shallow as 300 m below the sea surface (Armi et al. 1989; Käse and Zenk 1987). It is also worth noting that the meddy signals in this study are not necessarily individual meddies, but actually multiple meddies. Thus, this is observable from the residual height anomalies that are associated with several meddies passing by a given grid point in the monthly mean time series.

However, the question is how to remove the signals of the sea surface variation in the upper-layer η'_{UL}. The major component of the η'_{UL} is η'_T, which is not related to the signal of the meddies, but is related to upper-layer variations, including the Azores front, steric height, et cetera. Thus, the spatial resolution of the XBT data ($2° \times 5°$ latitude–longitude) to resolve mesoscale features was not high enough, and thus we used CPA (Fig. 2a) to convert SST to η'_T by applying a regression curve. The top, middle, and bottom panels in Fig. 2a are the first, second, and third spatial EOFs for
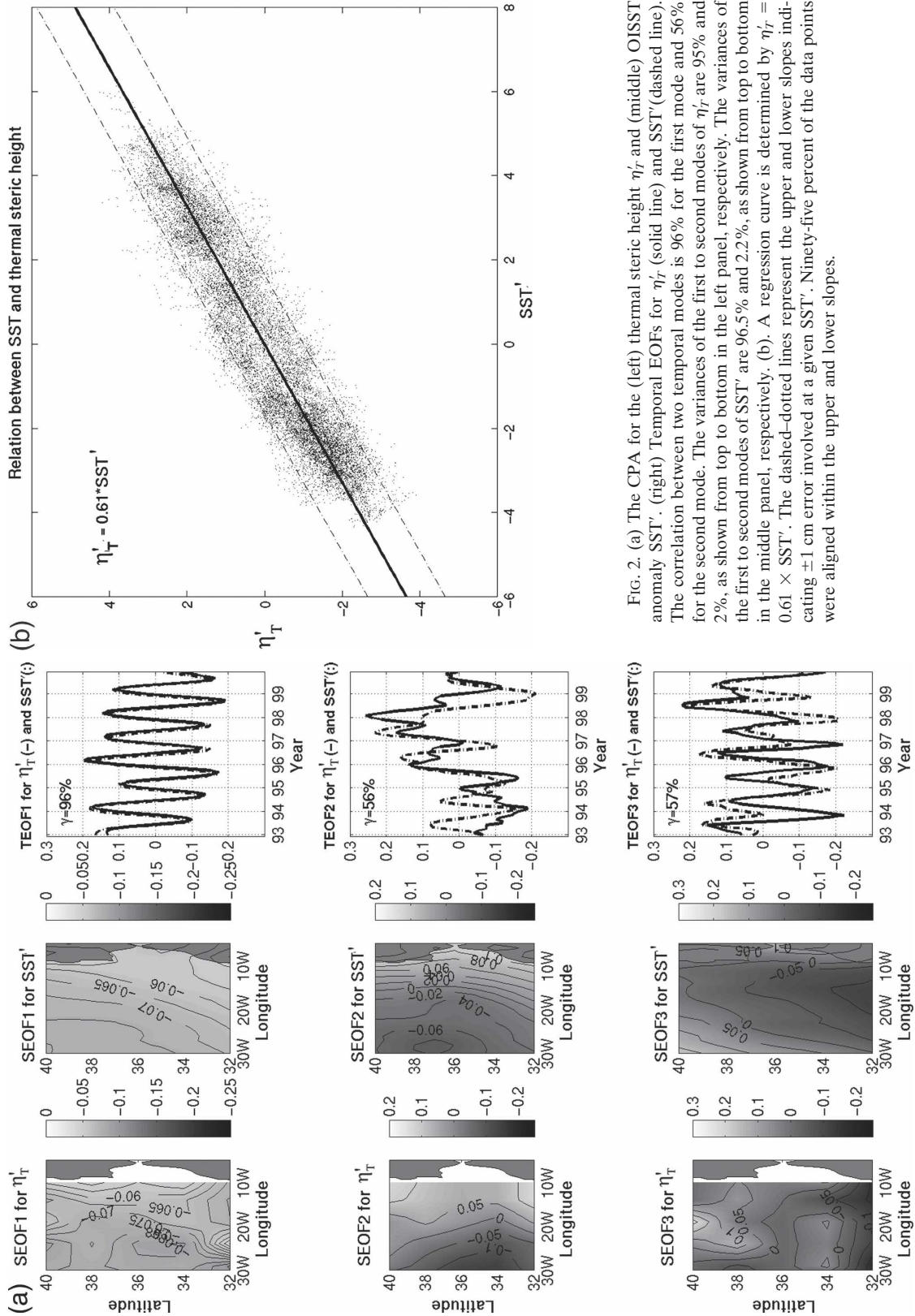
FIG. 2. (a) The CPA for the (left) thermal steric height η_T' and (middle) OISST anomaly SST'. (right) Temporal EOFs for η_T' (solid line) and SST' (dashed line). The correlation between two temporal modes is 96% for the first mode and 56% for the second mode. The variances of the first to second modes of η_T' are 95% and 2%, as shown from top to bottom in the left panel, respectively. The variances of the first to second modes of SST' are 96.5% and 2.2%, as shown from top to bottom in the middle panel, respectively. (b) A regression curve is determined by $\eta_T' = 0.61 \times$ SST'. The dashed–dotted lines represent the upper and lower slopes indicating ± 1 cm error involved at a given SST'. Ninety-five percent of the data points were aligned within the upper and lower slopes.

η'_T derived from the XBT measurements, the OISST anomaly, and temporal EOFs, respectively. From each spatial EOF, we can see the similarity of features. Furthermore, the correlations of temporal EOFs from the first to third modes between η'_T and the OISST anomaly are 96%, 66%, and 57%, respectively. Once we concluded that we can convert the OISST anomaly to the thermal steric height anomaly statistically, we determined a regression curve as $\eta'_T = 0.61 \times \text{SST}'$ (Fig. 2b) based on minimizing the $r^2_{x,t}$ [Eq. (8)]. This method was introduced by Leuliette and Wahr (1999). Similarly, we defined $f(x, t)$ in Eq. (4) as η'_T and $g(x, t)$ in Eq. (5) as the SST anomaly; that is,

$$r_{x,t} = f(x, t) - Ag(x, t). \qquad (8)$$

A conversion factor A was determined by least median of squares deviations $r_{x,t}$ to scale A to a depth H; that is, $H = A/\alpha$. Thus, the unit of the slope, 0.61, is centimeters per degree celsius. The mean error is approximately ±1 cm at a given SST' as shown with the upper and lower slopes (Fig. 2b). Last, the regression curve was applied to AVHRR SST (18 km) to obtain a new thermal steric height.

Because of the scarcity of temporal and spatial salinity data, we estimated the effect of η'_S in the upper layer indirectly. Using Levitus 94, the vertical structure of the salinity was examined to see the salinity distribution. The entire upper layer (above 400 m) in our study domain has a uniform salinity distribution (salinity variation around 0.2‰), except near 32°N, 18°W (salinity variation around 1‰). We concluded that the anomaly of η'_S is very small in the upper layer with only small variability at 32°N, 18°W. For instance, using conservation of mass, the contribution of the salinity can be estimated and compared with the meddy signal; that is,

$$\Delta\eta_S = \frac{\beta \times 0.2 \text{ psu} \times 400 \text{ m (upper layer)}}{\beta \times 1 \text{ psu} \times 800 \text{ m (meddy)}} \times 100 = 10\%. \qquad (9)$$

The characteristic salinity anomaly relative to the background is 1 psu and the thickness of a meddy is approximately 800 m. The salt expansion coefficient is β. Additionally, we compared vertical salinity data from the National Oceanographic Data Center (NODC) (18 September 1994; 36.3721°N, 29.67°W) with September Levitus 94 climatology data (Fig. 3). The mean salinity difference between the two dataset is 0.001 psu, and the standard deviation of the two datasets is 0.04 psu. The 0.001-psu difference between sea surface and 400-m depths contributes 0.12 cm to the sea surface change based on Eq. (9).

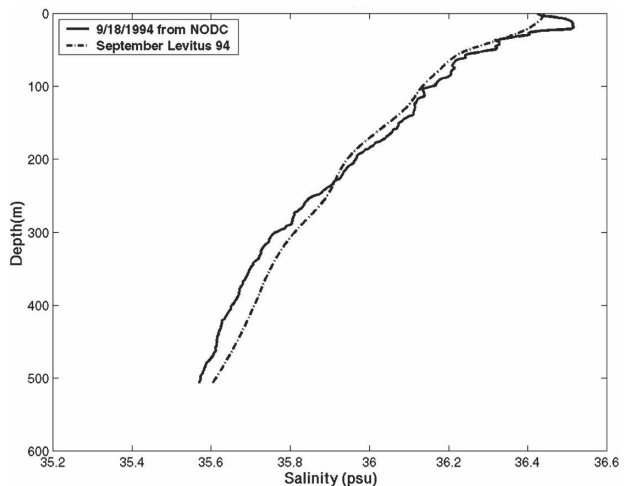The wind effect on the η'_{Total} signal was considered

FIG. 3. The solid line shows a vertical salinity obtained from NODC (18 Sep 1994; 36.3721°N, 29.67°W). The dashed–dotted line shows the Sep Levitus 94 climatological salinity. The mean salinity difference between the two dataset is 0.001 psu, and the standard deviation of the two datasets is 0.04 psu.

using scatterometer data. Initially we calculated correlations for the wind stress curl and the η'_{Total} to determine the temporal variation. A negative correlation would be expected, since rising sea level is associated with negative wind stress curl. The correlation coefficients showed about −30% in our study area with the southern area showing a larger rms than the northern area. Second, we considered the magnitude of the sea level variation due to wind stress based on a linear barotropic vorticity equation; that is,

$$\frac{d\eta}{dt} \approx \frac{-g'}{f0\rho g} \nabla \times \tau, \qquad (10)$$

where η is the sea level height, ρ is the water density, g' is the reduced gravity, f_0 is the Coriolis parameter, and τ is the wind stress. We also estimated η'_W using NSCAT (August 1996–June 1997) and QuikSCAT (June 1999–present). The mean sea level variation due to wind stress was less than 1 cm. This result agreed with the study of Greatbatch and Goulding (1989), who found a sea level variation (~0.5 cm) due to anomalous wind stress in this area. So this signal η'_W is less than 9% of the meddy signal [typically 6 cm; Stammer et al. (1991); Tychensky and Carton (1998)].

We used SSTs, determined from AVHRR (18-km resolution) data, to find the features of fronts, currents, and eddies. Then we compared them with our estimated meddy signals to determine the similarities of the features. The front has a thermal gradient of about 2°C and extends over a distance of 100 km. This gradient is visible across 34°N (Tychensky et al. 1998), and shows much more zonal variability (30 cm s^{-1}; Tychen-

sky et al. 1998) than is typically associated with meddy translation [$O(2–3 \text{ cm s}^{-1})$]. In addition, we compared the frontal features using a 15°C isothermal anomaly determined by XBT measurements $T'_{\text{iso15}°C}$, with both the sea surface features illustrated by altimeter data η'_{Total} and the sea level variation η'_T. The front features can be resolved by deriving thermal steric height and thus our new thermal steric height was derived from 18-km-resolution AVHRR data, and was then removed from the altimetry for the O&M computation. Accordingly, by removing the thermal steric height variation due to thermal variation and the front, this process (removal of η'_T) could be used to enhance the meddy signals at the isopycnal surface at the 400-m depth.

The mesoscale variability in the Azores–Madeura region is dominated by the Azores Current and its associated eddies, which have dominant scales larger than 300 km and 100 days (Le Traon and De Mey 1994). The surface eddies show larger diameters and shorter lifetimes than those of the meddies, and the surface eddies are much faster than the meddies. The characteristic temporal and spatial features are different from meddy signals.

We also examined the Rossby wave in the map of meddy signals. It has been reported that the westward-propagating Rossby wave features and characteristic wavelength and frequencies are ∼2.7, ∼1.6, and ∼0.8 km day^{-1} (Cipollini et al. 1997), and the period of the peak energy is reduced crossing the ridge from ∼1 yr to ∼7.9 months (Cromwell 2001). The two major peaks correspond to components of wavelength ∼1440 and ∼580 km, with periods of ∼330 and ∼220 days, respectively. Therefore, the characteristic temporal and spatial features are also different from meddy signals.

4. O&M signal and its validation

The result of $\Delta\eta' = \eta'_{\text{Total}} - \eta'_{\text{UL}}$ is apparently some variation of the vertical water column, which is a consequence of the different incoming or outgoing water masses under the upper layer. We can, therefore, investigate the pathways of the O&M in the North Atlantic by using data with better spatial and temporal resolution from space.

Data from the A Mediterranean Undercurrent Seeding Experiment (AMUSE; Bower et al. 1997) and Structures des Echanges Mer–Atmosphère, Propriétés des Hétérogénéités Océaniques: Recherche Expérimentale (SEMAPHORE; Richardson and Tychensky 1998) were used to confirm our estimation of the trajectories of the meddies and to study the variations of the meddies with time. The AMUSE data included an observational component based on the successful seeding, on a weekly basis, of a total of 49 RAFOS floats in the Mediterranean Undercurrent off southern Portugal, and 14 floats were embedded in meddies (Bower et al. 1997, their Table 2). The details of the data processing are described by Bower et al. (1997). The SEMAPHORE experiments using RAFOS floats showed 10 floats embedded in meddies (Richardson and Tychensky 1998, their Table 1). The details of the data processing for these experiments are described by Richardson and Tychensky (1998). During AMUSE, nine floats registered six meddy formation events in the vicinity of Cape St. Vincent and three at the Estremadura Promontory (Bower et al. 1997). Furthermore, six other floats revealed the presence of meddies as they were caught in the periphery of these structures.

For more validation of the meddies' location, the vertical temperature distribution measured at depths that reached 700 m was used. The individual XBT data were obtained from the NODC in the Global Temperature–Salinity Profile Program database (more information available online at http://www.nodc.noaa.gov/GTSPP/gtspp-bc.html). Out of the 298 XBT measurements in our study area during 1994, 121 measurements showed that the maximum depth of 700 m was exceeded. These 121 measurements were examined for meddy locations. Figure 4 shows the three different cases used to determine whether there was a meddy or not below 700-m depths. The first case (left panel in Fig. 4) implies that a meddy exists at depth (11 measurements found) determined by when the temperature difference of the deepest 100-m interval increases by 0.5°C or more, the second case (right panel in Fig. 4) implies that a meddy does not exist at depth (55 measurements found) when the temperature difference of the deepest 100-m interval decreases by 0.5°C or less, and the third case (middle panel in Fig. 4) implies an ambiguous case because of negligible temperature change (55 measurements found). Accordingly, the data from the first case were compared with meddy features determined by our method and by float observations in 1994. In fact, many studies showed the vertical temperature associated with the presence of a meddy (Tychensky and Carton 1998, their Plate 5; Richardson and Tychensky 1998, their Fig. 3; Schultz Tokos and Rossby 1991, their Fig. 2; Richardson et al. 1989, their Fig. 1).

To make comparisons in time between a real float trajectory, AM129, and our O&M signals, the trajectory of the AM129 is introduced in Fig. 5a. We can see an anticyclonic feature from the middle of March to September 1994. For more details on the meddy floats, one can refer to Bower et al.'s (1997) Table 2. For a specific comparison, we chose three points for floats
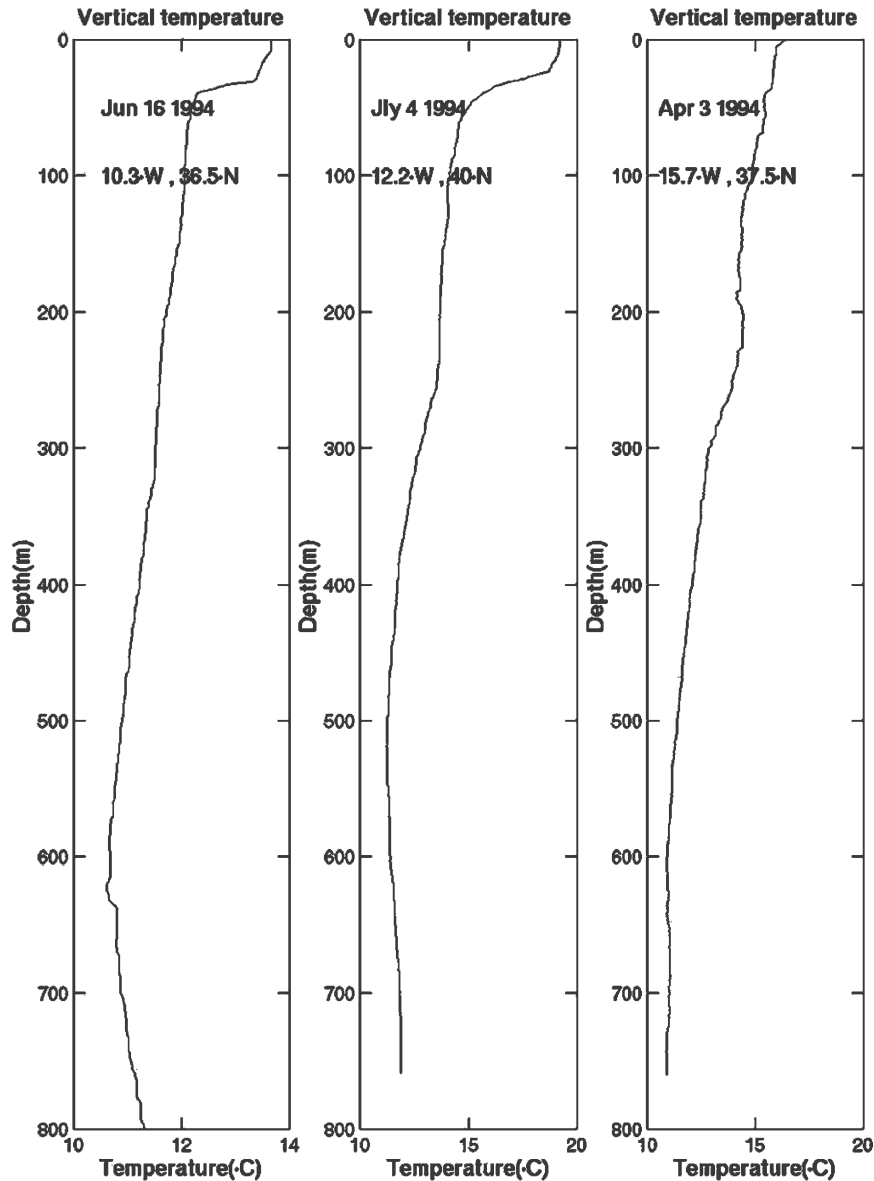
FIG. 4. Three different vertical temperature profiles from XBTs. (left) The first case is taken at 36°N, 10.3°W, on 16 Jun 1994. This case shows the meddy as a result of the temperature increase below 600 m. (middle) The second case is taken at 40°N, 12.2°W, on 4 Jul 1994 for the ambiguous case in which the temperature does not keep increasing below 600 m. (right) The third case is taken at 37.6°N, 15.7°W, on 3 Apr 1994. This case shows no meddy as a result of the temperature decrease or no change below 600 m.

(black squares) from each month and placed them on our O&M maps (Fig. 5b). The numbers represent the first, middle, and last days of the month. Our meddy signals are shown as relatively light areas in the gray-background map.

We believe the meddy signals in Fig. 5b are not an individual meddy, but actually multiple meddies. The conditions of the sequential vortices' (similarly med-dies) formation were reported by Cenedese and Linden

(1999) through laboratory experiments. Multiple vorti-ces were generated by a fast flow rate, and a single vortex was generated by a slow flow rate, which is why we can see relatively broad O&M features rather than an actual individual meddy. The other reason for the broad signals is that this method resolves the isopycnal surface at a depth of 400 m (Fig. 1), but not at 1000-m depth.

Figure 6 compares the annual O&M signals (gray
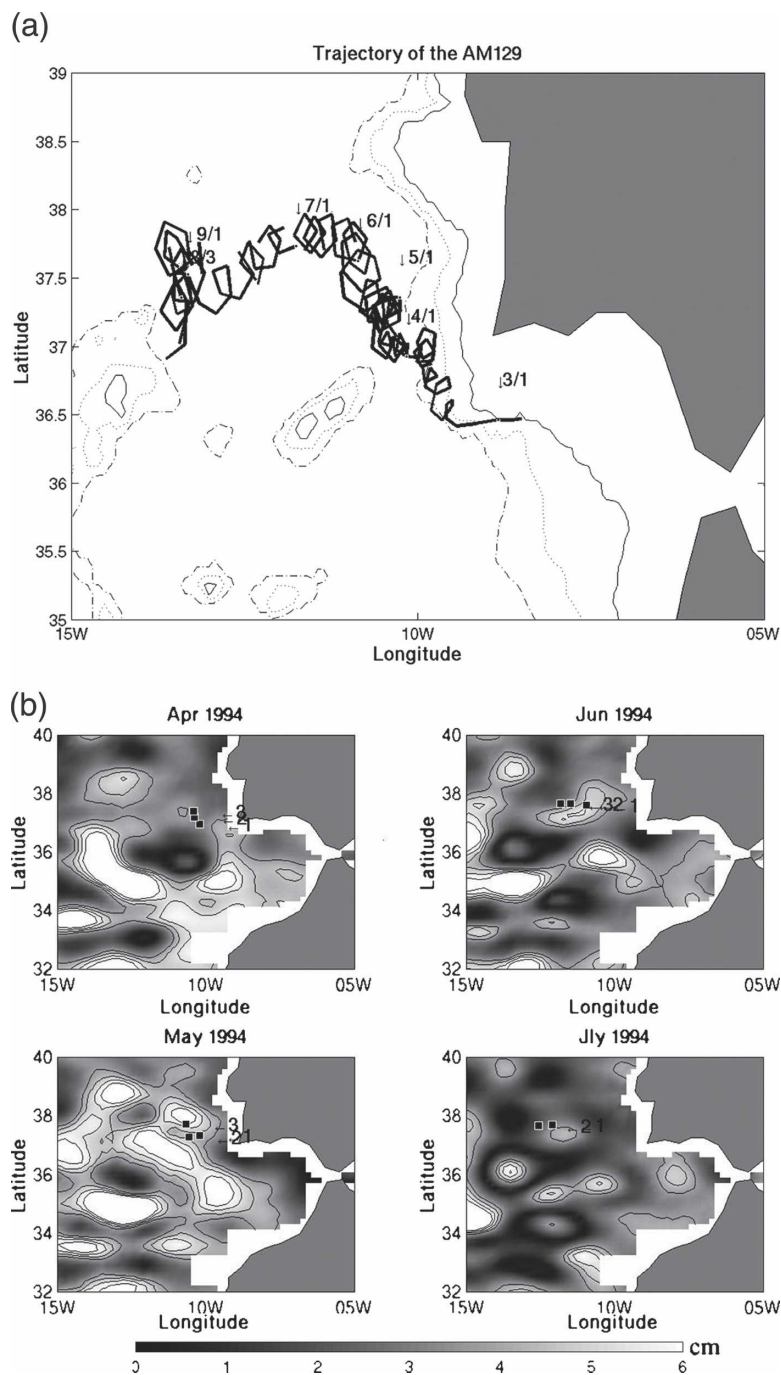
(a)

(b)

FIG. 5. (a) The trajectory of float AM129 from March to September 1994. The arrows indicate the first day of each month. The bathymetry is shown with different line styles [labeled at −1000- (dashed–dotted), −2000- (dotted), and −3000-m (solid) depths]. (b) The locations of float AM129 are overlain on a grayscale O&M map. The numbers (1, 2, and 3) represent the first, middle, and last day of each month, respectively.

map) with floats (black circles and diamonds). Most of floats are related to our high O&M signal. If we allowed 2–3-cm uncertainties on the meddy signals, then 72% (2 cm)–64% (3 cm) of the float observations agreed

with our results. It should be pointed out that in some locations in Fig. 6, for example, 35°N and 18°W in 1994, there are no black solid circles to compare or match with the meddy signal from our method. We believe
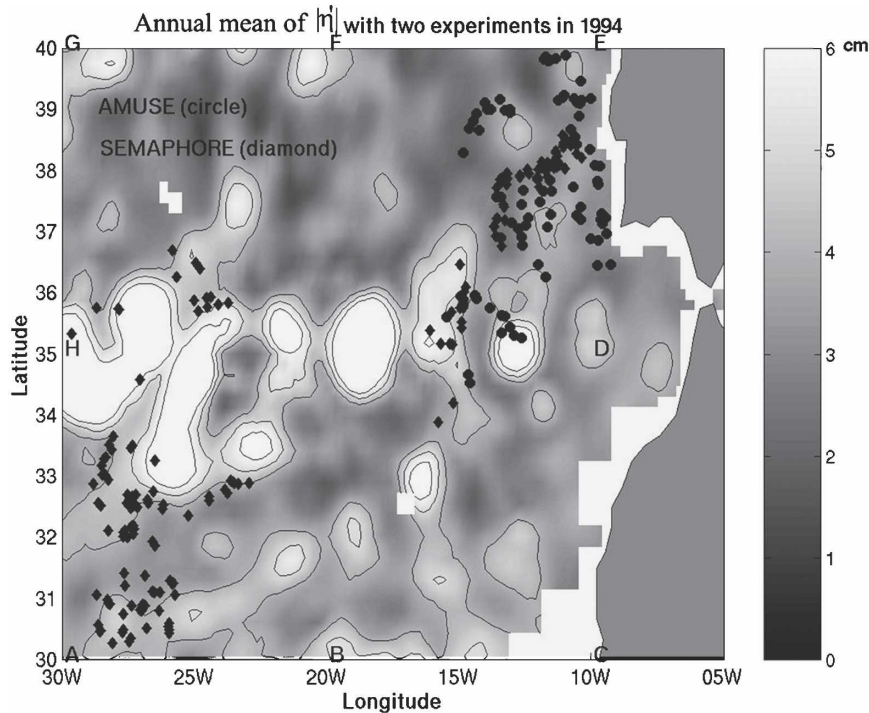
FIG. 6. Comparisons of annual mean $|\Delta\eta'|$ signal from two floats experiments in 1994. The grayscale and contours show the annual mean of the $|\Delta\eta'|$ signal estimated from our method. All meddies were discovered during AMUSE (solid circles) and SEMAPHORE (solid diamonds) in 1994.

this is simply because there were no floats or XBTs deployed at that location and time.

The direct comparison between our meddy map and both float trajectories of meddies and XBT vertical temperatures (Fig. 4) showed 80.3% agreement:

$$\text{Expected Value } (E_{ij}) = \frac{T_i \times T_j}{N}. \quad (11)$$

Furthermore, we conducted a statistical chi-square test to determine the degree of confidence of validation with in situ measurements. Using this statistical test, we can also show how reliable this method is. To determine the meddy signals (uncertain meddy signals) in our method, we considered the meddy signal (uncertain meddy signal) when our meddy signal was over 2 cm (below 2 cm). The uncertain meddy signals in Table 1 are defined as those with a meddy signal in our map of less than 2 cm, while floats and XBTs showed there were meddies. The first step in computing the chi-square test of independence is to compute the expected value for each cell under the assumption that the null hypothesis (H_0) is true: there are no differences between meddies in our map and meddies observed from floats and XBTs. Then, the hypothesis (H_1) for this

study is that there are differences between meddies in our map and meddies observed from floats and XBTs. The general formula for an expected cell value is as follows: where E_{ij} is the expected frequency for the cell in the ith row and the jth column, T_i is the total number of subjects in the ith row, T_j is the total number of subjects in the jth column, and N is the total number of subjects in the whole table. The general formula for the chi square is

$$\chi^2 = \sum \frac{(\text{Observed Value} - \text{Expected Value})^2}{\text{Expected Value}}. \quad (12)$$

TABLE 1. Chi-square test for the validation between meddies found using our method and meddies observed from field measurements.

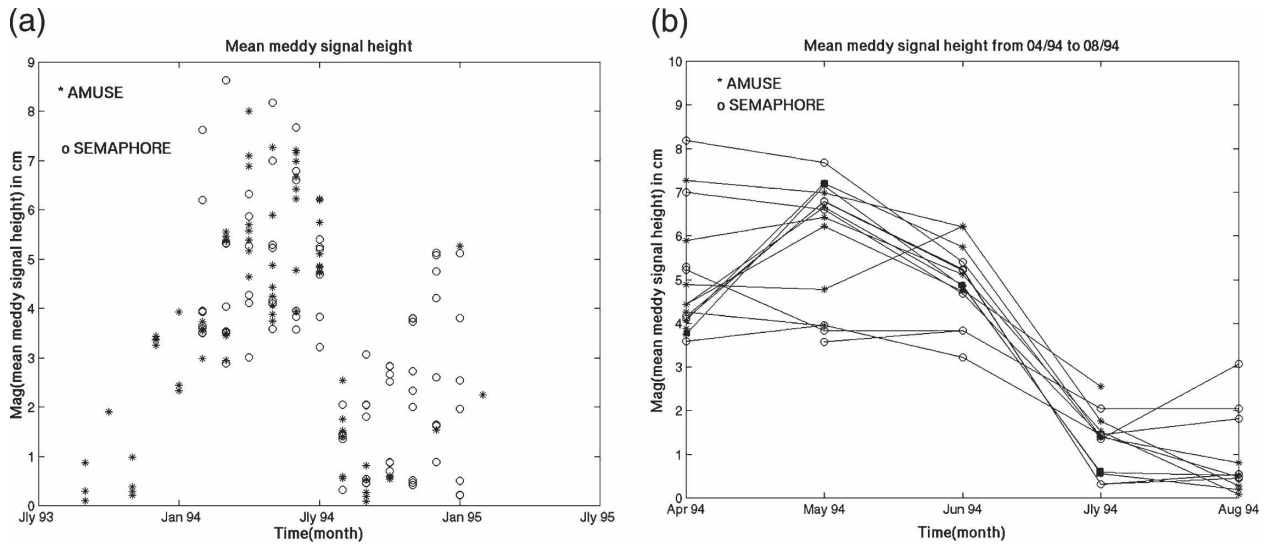| Our method	Meddies observed from floats	Meddies determined from XBTs	Total
Meddy signals	104	43	147
Uncertain signals	28	8	36
Total	132	51	183

FIG. 7. (a) Mean signal of the meddy (cm) [Eq. (13)] obtained from our method where the AMUSE and the SEMAPHORE experiments were available. The signal over 2 cm is considered to be significant. Note that the signals change because of uncertainties and the evolution of the meddies. (b) Mean signal of the meddies from April to August 1994, taken from Fig. 7a. The solid black squares are the mean signal over the AM129 float illustrated in Fig. 5b.

The number of degrees of freedom (df) is 1: df = $n -$ 1, where n is the number of classes. The obtained total probability (P value) is 0.6 for Table 1. In our chi-square test, the 0.05 probability level as our critical value corresponds to a 3.1 P value. Because the calculated chi-square value (or P value) is less than the criti-

cal value in the 95% significant level, we reject the hypothesis. Therefore, we accept the null hypothesis: there are no differences between meddies in our method and meddies observed from field observations.

Results from our method are classified into two categories based on the criterion of the 2-cm signal of the
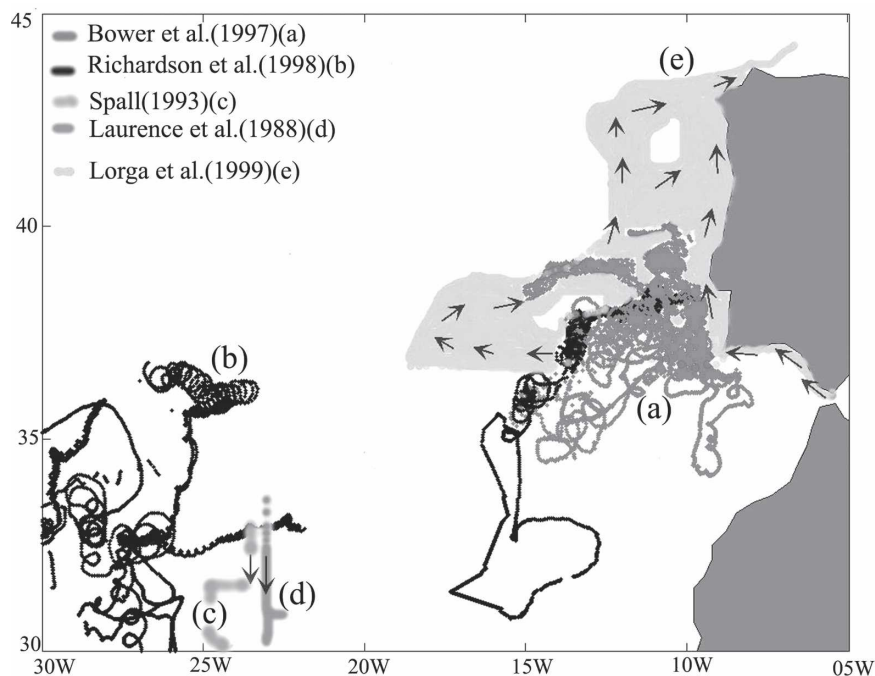

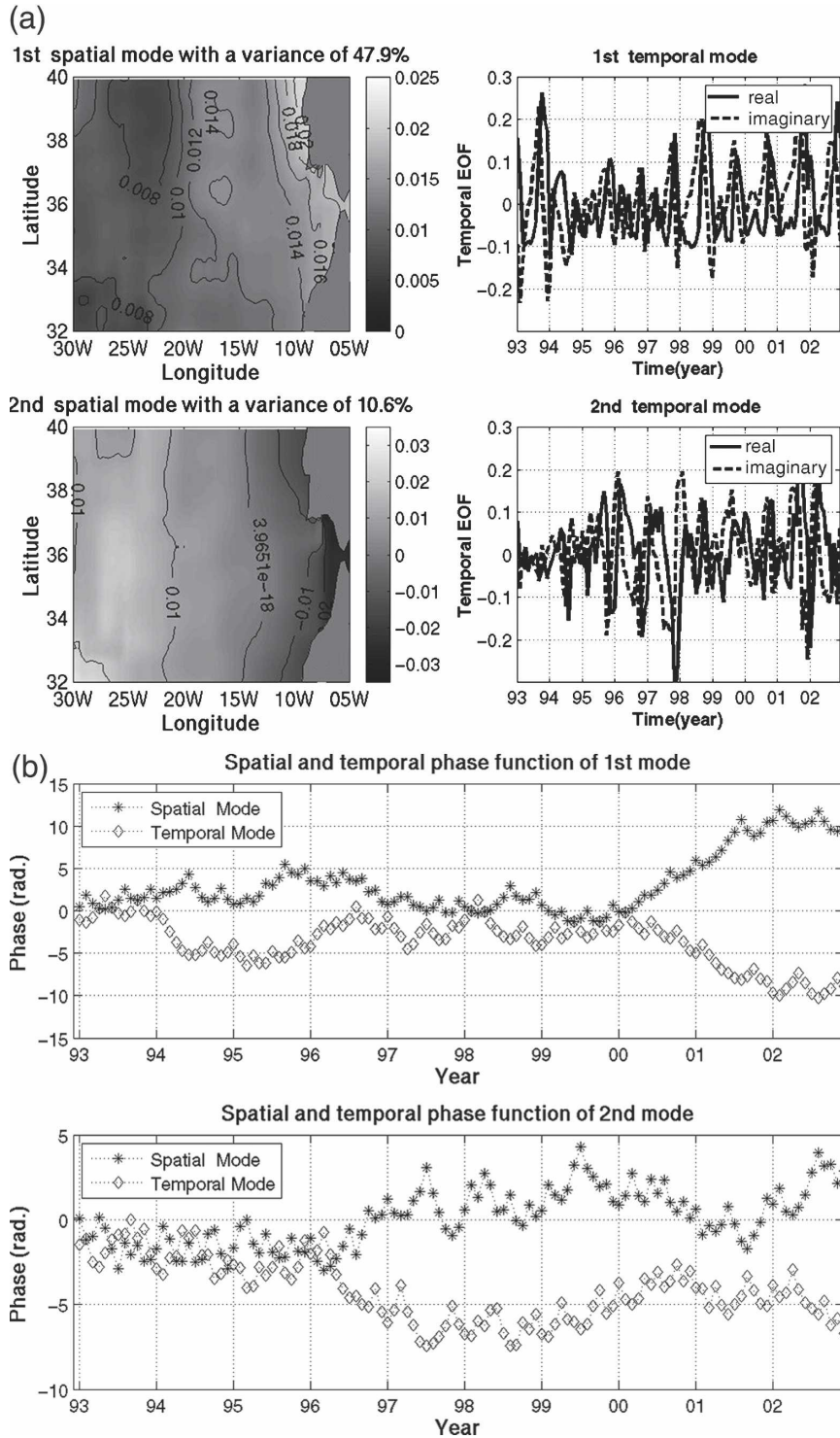FIG. 8. Five different comparisons of the meddy trajectories.

FIG. 9. (a) The first two spatial (left) and temporal (right) CSVDs of the $|\Delta\eta'|$ signals. The variances are 47.9% and 10.6% for the first and the second EOF modes, respectively. The spatial EOFs show the major locations of the O&M with each temporal variation. The first two temporal modes are shown in the right panel from top to bottom. The solid line represents the real part, and the dashed line represents the imaginary part. (b) Spatial and temporal phase functions of the first and second CSVD modes.

meddies: one is for the meddy signals (signals > 2 cm) validated by floats and XBTs (second row in Table 1), and the other is for the uncertain signals of our method (signals < 2 cm) while floats and XBTs showed there were meddies (third row in Table 1) determined by comparing our estimated O&M signals with floats and XBTs. From Table 1, the percentages of the significant meddy signals and uncertain meddy signals in our method are 80.3% (=147/183 × 100) and 19.7% (=36/183 × 100), respectively.

5. Analysis results

The annual comparison between field observations and our computation was very good and is shown in Fig. 6. In addition, Fig. 7a shows the monthly mean meddy signals, which were obtained for every float in each month ($t = 1$–n days). Therefore, we can estimate the relative magnitude of the O&M at the same place as the float trajectories in given months. This magnitude (M_{ag}) was computed using the monthly mean meddy signals from our method for each float during each month; that is,

$$M_{ab} = \sum_{l=1}^{n} |\Delta\eta'(T, S, W, X, t)|_l, \qquad (13)$$

where l represents the locations of the floats. The mean ranges were within 0–9 cm. We can see the time series of the meddy signal as being on the order of ~5 cm. Stammer et al. (1991) and Tychensky and Carton (1998) showed a similar order of magnitude (~6 cm). To demonstrate the variation of the O&M signals during specific periods, we plotted the mean O&M [Eq. (13)] from April to August 1994 in Fig. 7b. The black square represents the monthly mean magnitude of our meddy signals at the same place as the AM129 trajectories in given months as illustrated in Figs. 5a and 5b. The monthly mean meddy signals are 3.8, 7.4, 5, and 1.5 cm, from April to July, respectively. Each float has a different formation date and lifetime, but generally they are slowly decaying during these periods.

A comparison was also made with five studies, shown in Fig. 8. Bower et al. (1997) conducted experiments between May 1993 and March 1994, where 49 RAFOS floats were deployed in the Mediterranean Undercurrent off southern Portugal. These floats were acoustically tracked for up to 11 months and nine meddy formation events were observed: six near Cape St. Vincent, and three near the Estremadura Promontory along the western Portuguese continental slope. A meddy formation rate of 15–20 meddies per year was estimated. Richardson et al. (1989) estimated 8–12
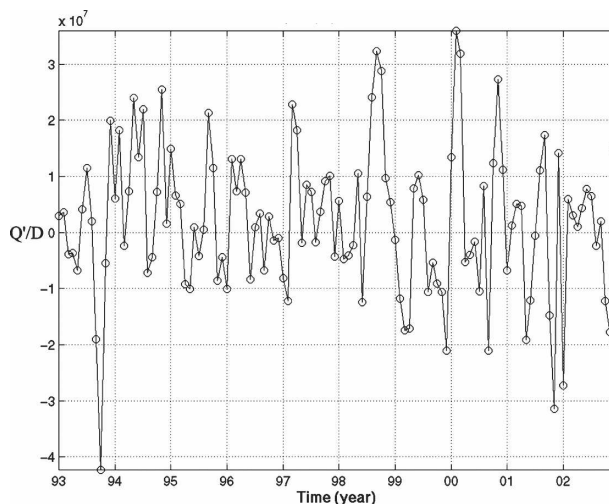

FIG. 10. Relative transport $[Q' = gD(\eta'|_{x2} - \eta'|_{x1})/f]$ over the Strait of Gibraltar.

meddies. The AMUSE meddies dispersed over the region between 33° and 42°N and between 7° and 17°W. Richardson and Tychensky (1998) obtained 10 meddy observations during the SEMAPHORE experiment. Spall et al. (1993) used SOFAR floats and observed a specific meddy in October 1984. Armi et al. (1989) showed Lagrangian trajectories from SOFAR floats, which were launched at 32°N, 24°W between 1984 and 1988. Iorga and Lozier (1999) used around 14 000 hydrographic stations in the North Atlantic, spanning the period 1904–90. They produced diagnostic modes in the eastern basin. Our study confirmed all the trajectories reported by the second and the third investigators. For the other studies, we could not make comparisons because there were no altimeter data available. As seen in the other studies, westward and southward meddies were observed in areas similar to those investigated during the period 1993–2002.

To study major spatial patterns of the O&M, we applied CSVD (Fig. 9a). The first two spatial EOFs account for 47.9% and 10.6% of the total variance, respectively. The high variation occurs in the major regions of the Mediterranean outflow, and the meddies' formation sites. The regions of small variation represent standing but oscillating features. The second spatial EOF shows high variation across 25°W, which has the inverse phase of Mediterranean outflow in the Gulf of Cadiz. The right panel of Fig. 9 shows the first and second temporal EOFs for a real part (solid line) and for an imaginary part (dashed line), respectively. The first spatial EOF shows a possible main trajectory of the O&M with annual signals with a maximum in boreal autumn and a minimum in boreal spring from the real
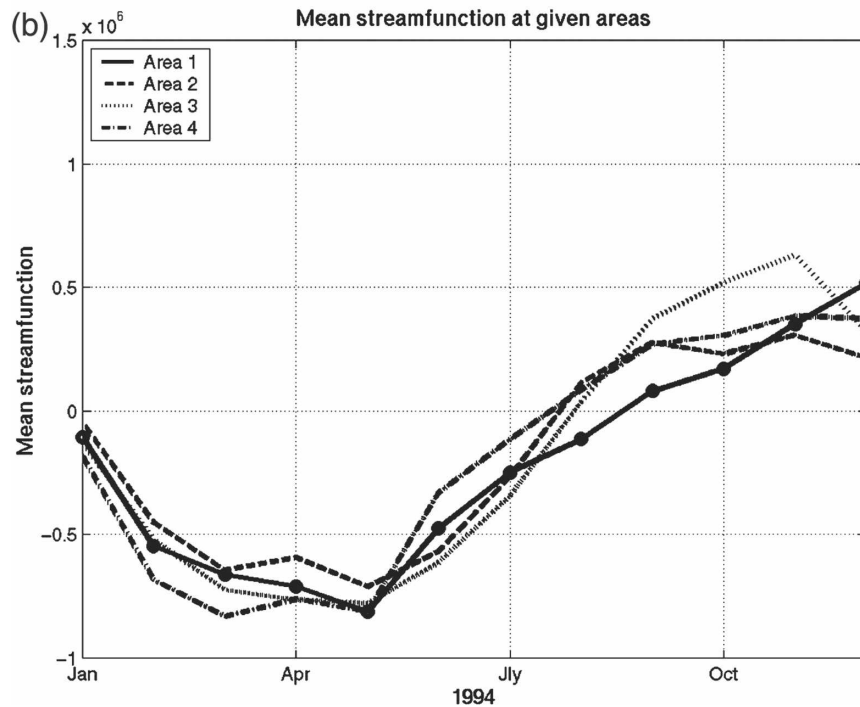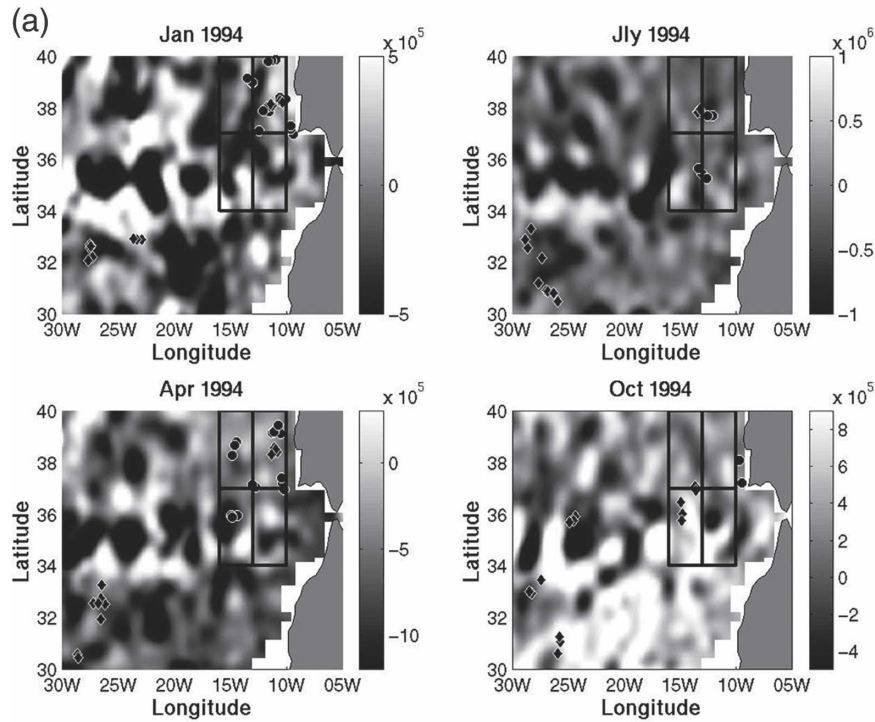
FIG. 11. (a) Comparisons of meddy trajectories with streamfunctions [Eq. (14)] for (top left) January, (bottom left) April, (top right) July, and (bottom right) October 1994. The solid circles represent floats during AMUSE, and the black diamonds represent floats during SEMAPHORE. The mean streamfunction is averaged over the four 3° × 3° boxes, and shown in Fig. 11b. (b) The time series of the four averaged streamfunctions over each box. Area 1 (solid boldface) is defined as 37°–40°N and 10°–13°W, area 2 (dashed boldface) is defined as 37°–40°N and 13°–16°W, area 3 (dotted) is defined as 33°–37°N and 13°–16°W, and area 4 (dashed–dotted) is defined by 33°–37°N and 10°–13°W, respectively.
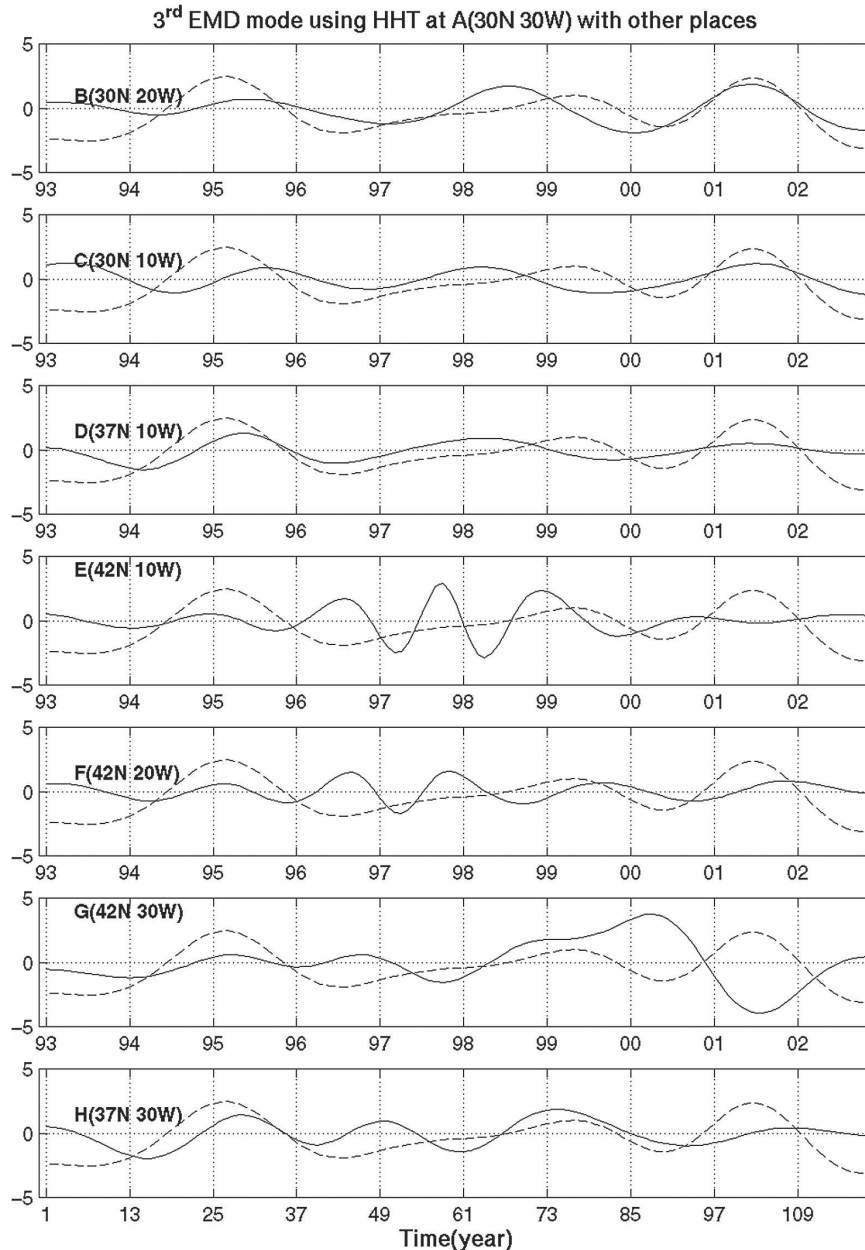
FIG. 12. (a) Comparisons of the third EMD modes using HHT are shown at given locations (B–H). For comparison, solid curve is for location A (refer to Fig. 6 for the location) in all panels. The dotted curve is for the individual EMD modes for those locations. (b) Time-frequency-spectrum-energy of the streamfunction at location A. Refer to Fig. 6 for location A. One can see the high energy for the 33-month period at location A, but not at location E. (c) Same as Fig. 12b but at location E.

part. Meanwhile, the phase changes with a maximum in boreal spring and a minimum in boreal autumn. When a maximum changes to a minimum, the spatial features are reversed, or vice versa.

Using Eq. (6) we computed the spatial and temporal function variations in terms of a wavenumber k and angular velocity ω (Fig. 9b). As Susanto et al. (1998)

demonstrated, the slope of the spatial function represents the wavenumber, and the slope of the temporal function represents the angular frequency. We could determine slopes after 2000 for the first spatial and temporal function as 0.4 and -0.4, respectively. Thus, the first CSVD shows the westward phase speed ($c = \omega/k$), -1 cm s^{-1}. Likewise, the second CSVD shows the
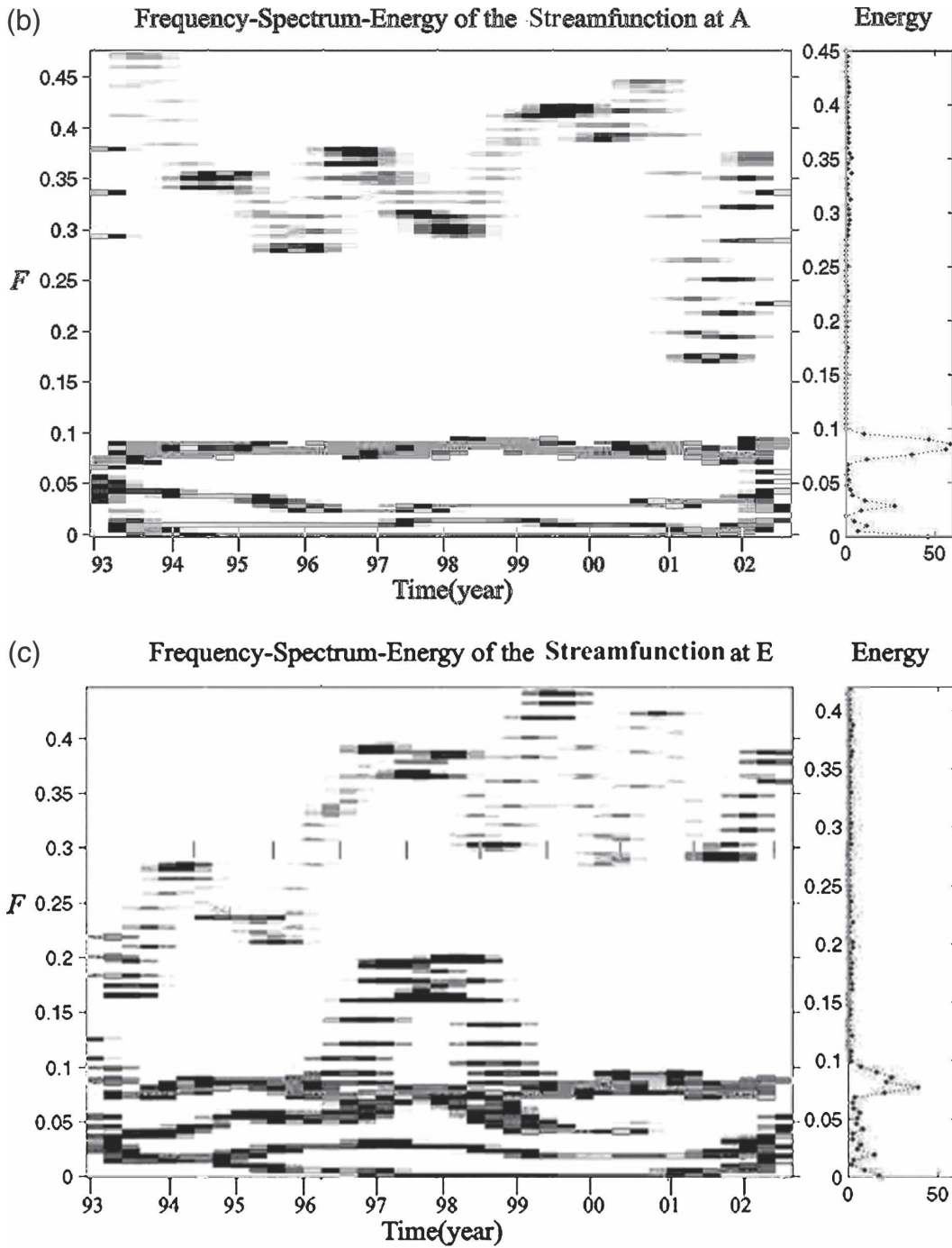
(b) Frequency-Spectrum-Energy of the Streamfunction at A — Energy

(c) Frequency-Spectrum-Energy of the Streamfunction at E — Energy

FIG. 12. (*Continued*)

phase speed varying from westward at -6.4 cm s^{-1} during July 1999–December 2001 to eastward at 2 cm s^{-1} in 2002 and thereafter. Other periods during this time frame show oscillatory changes when compared with the periods indicated above.

It is important to estimate how much salty Mediterranean water flows over the Strait of Gibraltar for the formation of O&M and thus to assess a salt budget in the North Atlantic. In Fig. 10, the relative transport $Q' = gD(\eta'|_{x2} - \eta'|_{x1})/f$ is shown between the 6°W cross section on the west side of the Strait of Gibraltar and the 5°W cross section on the east side of the Strait of Gibraltar. In addition, g is the gravitational acceleration, D is the depth, f is the Coriolis force, and $\eta'|_{x2}$ and

$\eta'|_{x1}$ are the sea level variations at places x_2 and x_1, respectively. Because the exact thickness of the O&M cannot be estimated, we computed Q'/D with respect to time. We can interpret Fig. 10 as follows: if there is more salty Mediterranean water over the Strait of Gibraltar, the salt steric height decreases, which thus decreases the total sea surface height. The Mediterranean water, which can be dense because of evaporation in the eastern basin, flows westward below the surface along the western Mediterranean Sea and out through the Strait of Gibraltar into the Atlantic. The opposite holds for the positive relative anomaly during wintertime.

To investigate the reasons for the change in the direction of propagation of meddies with respect to sea surface variation, the streamfunction ψ was computed using the altimetry. This representation of the streamfunction allows observations of the interactions between the sea surface gradient and the meddies' propagation. The computation of the sea surface height anomaly η' in terms of the usual dynamic variables is straightforward if the flow is assumed to be quasigeostrophic: the streamfunction ψ is defined as

$$\psi = \frac{g}{f_0} \eta'_{\text{Total}}, \tag{14}$$

where ψ is the surface quasigeostrophic streamfunction (e.g., Douglas et al. 1983).

This is illustrated to examine the seasonal migration of the tropical water moving toward the north and polar water moving toward south over the O&M signals (Fig. 11a). Because most of meddies are generated near Cape St. Vincent at the southwestern corner of the Iberian Peninsula, we made four $3° \times 3°$ boxes along $37°N$ to understand the response of the O&M due to changes of sea surface pressure gradients (Fig. 11a). Figure 11b shows the time series of the averaged streamfunction over each box. From January to May 1994, high sea surface height in area 2 produces a pressure gradient toward area 4. Similarly, from May to August, there is a pressure gradient from area 4 to area 3; from August to November, there is a pressure gradient from area 3 to area 1, respectively. We compared the meddies measured by the floats and the streamfunctions in all the months in the experimental periods and found that the meddies preferred to travel toward the low streamlines and stayed within the northernmost and southernmost streamlines in April and October, respectively.

To find out the dominant signal of the sea surface interaction with the meddies, the HHT was applied to their EMD modes. We chose eight places to investigate the dominant signal in our study area. Figure 12a shows that place groups 1 (B, C, and D, shown in Fig. 6) and

2 (H and G, shown in Fig. 6) have similar signals. However, group 3 (E and F, shown in Fig. 6) has a slightly different signal from groups 1 and 2. Consequently, there were seasonal fluctuations between location A and group 3. To compute the dominant signal of the power for locations A and E, the HHT was employed and is shown in Figs. 12b and 12c. In both, the dominant frequency F was around $F = 0.082$ (1 yr). However, location A had a lower frequency, 0.03 (33.3 months), which seems to indicate that wind stress with 33.3-month period produces sea surface forcing. The surface variations produce the baroclinic instability on the meddies, which is related to southward translation. The southward translation of the meddies due to the baroclinic effects was consistent with that discussed by Müler and Siedler (1992) and by Käse and Zenk (1996). If the current is vertically sheared in a stratified fluid, baroclinic instability can occur.

6. Conclusions

In analyzing the trajectories of O&M, sea surface height anomalies were calculated and examined using satellite altimetry, IR satellite imagery, XBT temperature fields, and scatterometer wind measurements. Satellite observations provided a good way to overcome the limitations of the spatial and temporal coverage of field measurements. Using spaceborne measurements, we have shown the spatial and temporal variations of the O&M trajectories in the North Atlantic Ocean. The validations were conducted using data from the AMUSE and the SEMAPHORE experiments and XBT measurements for the vertical temperature distribution. Most of the floats and XBTs' meddy cases were located in the high signal areas of the O&M map we produced.

We also calculated the relative transport of salty Mediterranean water over the Strait of Gibraltar. We found that saltier water from the Mediterranean Sea was transported into the North Atlantic in boreal spring and summer relative to boreal autumn and winter. The meddies' propagating directions were related to sea surface geostrophic flow, and the meddies were confined within the north and south boundaries, which revealed seasonal variability. Meddies tended to travel toward low streamlines, because of the pressure of the surface pushing the meddies toward the low pressure areas. Interpolation and wind stress errors could cause possible error in this study, but they were not significant in comparison with the real signals. We believe that this is an improved effort (studying a very interesting phenomenon at the 400-m-depth isopycnal surface from space) that has been achieved successfully using state-of-the-art satellite multisensor remote sensing data.

REFERENCES

Armi, L., and H. Stommel, 1983: Four views of a portion of the North Atlantic subtropical gyre. *J. Phys. Oceanogr.,* **13,** 828–857.

——, and W. Zenk, 1984: Large lenses of highly saline Mediterranean salt lens. *J. Phys. Oceanogr.,* **14,** 1560–1576.

——, D. Hebert, N. Oakey, J. Price, P. Richardson, T. Rossby, and B. Ruddick, 1989: Two years in the life of a Mediterranean salt lens. *J. Phys. Oceanogr.,* **19,** 354–370.

Barnett, T. P., 1983: Interaction of the monsoon and Pacific trade wind systems at interannual time scales. Part I: The equatorial zone. *Mon. Wea. Rev.,* **111,** 756–773.

Bower, A. S., L. Armi, and I. Ambar, 1997: Lagrangian observations of eddy formation during A Mediterranean Undercurrent Seeding Experiment. *J. Phys. Oceanogr.,* **27,** 2545–2575.

Bretherton, C. S., C. Smith, and J. M. Wallace, 1992: An intercomparison of methods for finding coupled patterns in climate data. *J. Climate,* **5,** 541–560.

Cenedese, C., and P. F. Linden, 1999: Cyclone and anticyclone formation in a rotating stratified fluid over a sloping bottom. *J. Fluid Mech.,* **381,** 199–223.

Cipollini, P., D. Cromwell, M. S. Jones, G. D. Quartly, and P. G. Challenor, 1997: Concurrent altimeter and infrared observations of Rossby wave propagation near 34°N in the northeast Atlantic. *Geophys. Res. Lett.,* **24,** 889–892.

Cromwell, D., 2001: Sea surface height observations of the 34°N "waveguide" in the North Atlantic. *Geophys. Res. Lett.,* **28,** 3705–3708.

Douglas, B. C., R. E. Cheney, and R. W. Agreen, 1983: Eddy energy of the northwest Atlantic and Gulf of Mexico determined from GEOS 3 altimetry. *J. Geophys. Res.,* **88,** 9595–9603.

Greatbatch, R., and A. Goulding, 1989: Seasonal variations in a linear barotropic model of the North Atlantic driven by the Hellerman and Rosenstein wind stress field. *J. Phys. Oceanogr.,* **19,** 572–595.

Huang, N., and Coauthors, 1998: The empirical mode decomposition and Hilbert spectrum for nonlinear and nonstationary time series analysis. *Proc. Roy. Soc. Math., Phys. Eng. Sci.,* **454,** 903–995.

Iorga, M. C., and M. S. Lozier, 1999: Signature of the Mediterranean outflow from a North Atlantic climatology, 1. Salinity and density fields. *J. Geophys. Res.,* **104,** 25 985–26 009.

Käse, R. H., and W. Zenk, 1987: Reconstructed Mediterranean salt lens trajectories. *J. Phys. Oceanogr.,* **17,** 158–163.

——, and ——, 1996: Structure of the Mediterranean Water and meddy characteristics in the northeastern Atlantic. *Ocean Circulation and Climate (Observation and Modeling the Global Ocean),* W. Krauss, Ed., Gebr. Borntraeger, 365–395.

Le Traon, P. Y., and P. De Mey, 1994: The eddy field associated with the Azores Front east of the Mid-Atlantic Ridge as observed by the *Geosat* altimeter. *J. Geophys. Res.,* **99,** 9907–9923.

Leuliette, E. W., and J. M. Wahr, 1999: Coupled pattern analysis of sea surface temperature and TOPEX/Poseidon sea surface height. *J. Phys. Oceanor.,* **29,** 599–611.

Levitus, S., and T. P. Boyer, 1994: *Temperature.* Vol. 4, *World Ocean Atlas,* NOAA Atlas NESDIS 4, 117 pp.

McDowell, S., and H. Rossby, 1978: Mediterranean Water: An intense mesoscale eddy off the Bahamas. *Science,* **202,** 1085–1087.

Müler, T. J., and G. Siedler, 1992: Multi-year current time series in the eastern North Atlantic Ocean. *J. Mar. Res.,* **50,** 63–98.

Oliveira, P. B., A. Nuno Serra, F. G. Fiuza, and I. Ambar, 2000: A study of meddies using simultaneous in-situ and satellite observations. *Satellites, Oceanography and Society,* D. Halpern, Ed., Elsevier Oceaongraphy Series, Elsevier, 125–148.

Peng, S., and J. Fyfe, 1996: The coupled pattern between sea level pressure and sea surface temperature in the midlatitude North Atlantic. *J. Climate,* **9,** 1824–1839.

Pingree, R., and B. Le Cann, 1992: Three anticyclonic slope water oceanic eddies (SWODDIES) in the southern Bay of Biscay in 1990. *Deep-Sea Res.,* **39,** 1147–1175.

——, and ——, 1993: A shallow meddy (a smeddy) from the secondary Mediterranean salinity maximum. *J. Geophys. Res.,* **98,** 20 169–20 185.

Reynolds, R. W., and T. M. Smith, 1994: Improved global sea surface temperature analyses using optimum interpolation. *J. Climate,* **7,** 929–948.

Richardson, P. L., and A. Tychensky, 1998: Meddy trajectories in the Canary Basin measured during the SEMAPHORE experiment, 1993–1995. *J. Geophys. Res.,* **103,** 25 029–25 045.

——, D. Walsh, L. Armi, M. Schröder, and J. F. Price, 1989: Tracking three meddies with SOFAR floats. *J. Phys. Oceanogr.,* **19,** 371–383.

——, A. S. Bower, and W. Zenk, 2000: A census of meddies tracked by fronts. *Progress in Oceanography,* Vol. 45, Pergamon, 209–250.

Schultz Tokos, K. L., and T. Rossby, 1991: Kinematics and dynamics of a Mediterranean salt lens. *J. Phys. Oceanogr.,* **21,** 879–892.

Spall, M. A., P. L. Richardson, and J. Price, 1993: Advection and eddy mixing in the Mediterranean salt tongue. *J. Mar. Res.,* **51,** 797–818.

Stammer, D., H. H. Hinrichsen, and R. H. Käse, 1991: Can meddies be detected by satellite altimetry? *J. Geophys. Res.,* **96,** 7005–7014.

Susanto, R. D., Q. Zheng, and X.-H. Yan, 1998: Complex singular value decomposition analysis of equatorial waves in the Pacific observed by TOPEX/Poseidon altimeter. *J. Atmos. Oceanic Technol.,* **15,** 764–774.

Tokmakian, R. T., and P. G. Challenor, 1993: Observations in the

Canary Basin and the Azores frontal region using Geosat data. *J. Geophys. Res.,* **98,** 4761–4773.

Tychensky, A., and X. Carton, 1998: Hydrological and dynamical characterization of meddies in the Azores region: A paradigm for baroclinic vortex dynamics. *J. Geophys. Res.,* **103,** 25 061–25 079.

——, P.-Y. Le Traon, F. Hernanez, and D. Jourdan, 1998: Large structures and temporal change in the Azores front during the SEMAPHORE experiment. *J. Geophys. Res.,* **103,** 25 009–25 027.

Wallace, J. M., C. Smith, and C. S. Bretherton, 1992: Singular value decomposition of wintertime sea surface temperature and 500-mb height anomalies. *J. Climate,* **5,** 561–576.

Wilson, W., and D. Bradley, 1966: Specific volume, thermal expansion and isothermal compressibility of seawater. U.S. Naval Ordnance Laboratory Tech. Rep. 66-103.

Yan, X.-H., and A. Okubo, 1992: Three-dimensional analytical model for the mixed layer depth. *J. Geophys. Res.,* **97,** 20 201–20 226.

——, J. R. Schubel, and D. W. Pritchard, 1990: Oceanic upper mixed layer depth determination by the use of satellite data. *Remote Sens. Environ.,* **32,** 55–74.

——, A. Okubo, J. R. Shubel, and D. W. Pritchard, 1991a: An analytical mixed layer remote sensing model. *Deep-Sea Res.,* **38,** 267–287.

——, P. P. Niller, and R. H. Stewart, 1991b: Construction and accuracy analysis of images of the daily-mean mixed layer depth. *Int. J. Remote Sens.,* **12,** 2573–2584.